Inorganic Chemistry

ARTICLE

pubs.acs.org/IC

Utilizing the Adaptive Polyoxometalate $[As_2W_{19}O_{67}(H_2O)]^{14-}$ To Support a Polynuclear Lanthanoid-Based Single-Molecule Magnet

Chris Ritchie,[†] Manfred Speldrich,[‡] Robert W. Gable,[†] Lorenzo Sorace,[§] Paul Kögerler,[‡] and Colette Boskovic*[,†]

[†]School of Chemistry, University of Melbourne, Victoria, 3010, Australia

[‡]Institute of Inorganic Chemistry, RWTH Aachen University, D-52074 Aachen, Germany

[§]Laboratory for Molecular Magnetism, INSTM RU and Department of Chemistry "U. Schiff", University of Florence, Via della Lastruccia 3-13, 50019 Sesto Fiorentino (FI), Italy

Supporting Information

ABSTRACT: Five members of a new family of polyoxometalate (POM)-ligated tetranuclear rare earth metal complexes have been synthesized and characterized. These compounds have the general formula $(HDABCO)_8H_5Li_8[Ln_4As_5W_{40}O_{144}(H_2O)_{10}(gly)_2]\cdot 25H_2O$ [Ln = Gd (**1**), Tb (**2**), Dy (**3**), Ho (**4**) and Y = (**5**), HDABCO = monoprotonated 1,4-diazabicyclooctane, gly = glycine] and were synthesized from the preformed POM precursor $[As_2W_{19}O_{67}(H_2O)]^{14-}$. The structure is comprised of two $\{As_2W_{19}O_{68}\}$ building blocks linked by a unit containing four rare earth ions and two additional tungsten centers, with the two glycine ligands playing a key bridging role. Two crystallographically distinct rare earth ions are present in each complex, both of which possess axially compressed, approximate square antiprismatic coordination geometry. The variable-temperature magnetic susceptibility profiles for **2**−**4** are dominated by population/depopulation of the M_J sublevels of the relevant ground terms, and fitting of the data has afforded the ligand field parameters in each case, from which the energies of the M_J sublevels can be calculated. Alternating current magnetic susceptibility data have revealed the onset of slow magnetic relaxation for **3**, with the energy barrier to magnetization reversal determined to be 3.9(1) K. As for other lanthanoid complexes that display slow magnetic relaxation, this energy barrier is due to the splitting of the M_J sublevels of the Dy^{3+} ions such that the ground sublevel has a relatively large $|M_J|$ value, thereby affording Ising-type magnetic anisotropy. This complex is thus the first POM-supported polynuclear lanthanoid-based SMM. Simulation of the W-band EPR spectrum of **1** has afforded the spin Hamiltonian parameters for this species, while the X-band EPR spectrum of **3** indicates the presence of a non-negligible fourth-order transverse component of the anisotropy, which is responsible for the small effective energy barrier observed for **3** and the absence of slow magnetic relaxation for **4**.

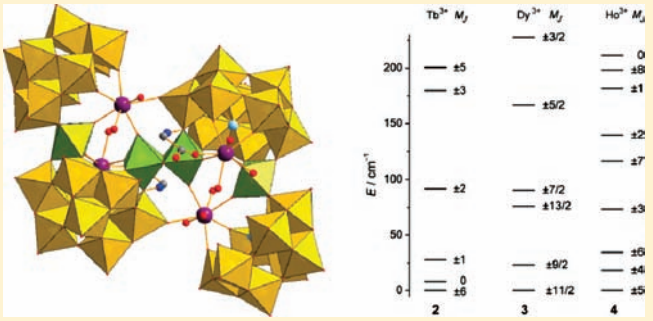

INTRODUCTION

Polyoxometalates (POMs) are polynuclear metal−oxygen complexes of the early transition metals that are comprised of assemblies of metal-centered MO_n polyhedra linked by shared corners, edges, or faces, sometimes with additional heteroatoms incorporated within the cluster.[1] As a class of inorganic compounds they possess an exceptional range of both structural and compositional diversity, allowing tuning of their electronic structure and consequently their potential functionality.[2] Due to this range of properties, POM-containing species have found application in catalysis, materials science, and medicine.[3] The oxygen-rich surface of POMs renders them excellent inorganic ligands for oxophilic d- and f-block metals, giving rise to a wide variety of coordination complexes.[4]

Beyond investigations into the magnetic behavior of reduced POMs[5] and POM-ligated complexes of open-shell transition metal or lanthanoid metal centers,[6] significant scope remains for the design of magnetically interesting materials based on POMs. Thus, recent reports of the first POM-supported single-molecule magnets (SMMs) suggests considerable promise for important new developments in this area.[7−9] The chemistry and physics of SMMs has been well established for some time, with many examples of polynuclear complexes of paramagnetic transition metals showing slow magnetic relaxation that is of molecular origin.[10] This slow relaxation is a consequence of an anisotropy-induced energy barrier to magnetization reversal that arises from the zero-field splitting of the molecular ground state (i.e., an energy barrier between $\pm M_S$ substates). More recently, similar slow magnetic relaxation has been observed for lanthanoid

Received: February 21, 2011
Published: July 06, 2011

complexes,[11] first for mononuclear complexes such as the $[Pc_2Ln]^-$ family (Pc = phthalocyanine)[12,13] and subsequently for polynuclear species.[14] The origin of the energy barrier to magnetization reversal in these cases is again of molecular origin but associated with the ligand field splitting of the ground electronic term of the lanthanoid single ions (i.e., an energy barrier between $\pm M_J$ substates). As a result, this subset of SMMs may also be referred to as "single-ion magnets". In addition to SMMs that contain solely d-block or f-block metals, some mixed 3d−4f complexes also display SMM behavior.[15] However, regardless of the nature of the metal center, organic ligands have generally been used to bridge these metals together and also to act synthetically as "blocking ligands" by preventing further agglomeration to extended systems. Thus, the novelty of the SMMs $[\{Mn_6O_4(H_2O)_4\}\{XW_9O_{34}\}_2]^{12-}$ (X = Si and Ge),[7] $[Fe_4(H_2O)_2(FeW_9O_{34})_2]^{10-}$, $[(Fe_4W_9O_{34}(H_2O))_2(FeW_6O_{26})]^{19-}$,[9] $[Ln(W_5O_{18})_2]^{9-}$ (Ln = Ho and Er), and $[Ln(\beta_2\text{-}SiW_{11}O_{39})_2]^{13-}$ (Ln = Dy, Ho, Er and Yb)[8] arises from their employment of diamagnetic inorganic POM ligands to support the polynuclear Mn- and Fe-based SMMs on the one hand and the mononuclear Ln-based species on the other. Their size and chemistry renders POMs particularly promising supporting ligands for SMMs because their steric bulk minimizes dipole-dipole coupling between neighboring molecules. In addition, they can be prepared as nuclear spin-free systems, with nuclear spin a major source of the quantum decoherence that would be detrimental to the use of SMMs in quantum computing.

Exploration of the chemistry of polynuclear rare earth complexes with POM ligands is an ongoing pursuit in our research group.[16−19] Synthetically, the highly oxophilic nature of the rare earth metals often impedes isolation of single crystals of rare earth-containing POMs, with rapid precipitation of insoluble amorphous materials a common occurrence. Nevertheless, some of the compounds that have been crystallographically characterized include a number of the largest and most complicated POM structural motifs to date, such as the nanoscopic molecules $[Ce_{16}As_{12}(H_2O)_{36}W_{148}O_{524}]^{76-}$,[20] $[(Eu_2PW_{10}O_{38})_4(W_3O_8(H_2O)_2(OH)_4]^{22-}$,[21] and the 3D framework $\{Ln_4(H_2O)_{28}[KP_8W_{48}O_{184}(H_4W_4O_{12})_2Ln_2(H_2O)_{10}]^{13-}\}_n$ (Ln = La, Ce, Pr, Nd).[22] Our own efforts in this direction have afforded the 1D chain complex $[Nd_3As_4W_{41}O_{141}(OH)(H_2O)_{10}]_n^{16-}$ and the 0D family $[Cs\subset Ln_6As_6W_{63}O_{218}(H_2O)_{14}(OH)_4]^{25-}$ (Ln = Eu, Gd, Tb, Dy, Ho, and Er).[17,18] A particular focus of our research has involved combining organic carboxylate-containing ligands with lacunary POM ligands to afford the 1D chain species $[Dy_4As_2W_{22}O_{76}(H_2O)_{19}(gly)_2]_n^{2-}$ and the discrete complexes $[Gd_6As_6W_{65}O_{229}(OH)_4(H_2O)_{12}(OAc)_2]^{38-}$, $[Yb_{10}As_{10}W_{88}O_{308}(OH)_8(H_2O)_{28}(OAc)_4]^{40-}$, $[Tb_4As_2W_{19}O(H_2O)_2(pic)_4]^{10-}$, and $[Tb_8As_4W_{38}O_{132}(H_2O)_{22}(pic)_{12}]^{12-}$ (OAc = acetate, pic =2-picolinate).[16,18,19] The octanuclear Tb^{3+} complex is of particular interest as it displays strong picolinate-sensitized, Tb-based green luminescence.[19] While carboxylate-containing ligands are not so unusual in POM chemistry, amino acids have been little employed in this capacity, with $[Ce_4As_4W_{44}O_{151}(ala)_4(OH)_2(H_2O)_{10}]^{12-}$ and $[Dy_4As_2W_{22}O_{76}(H_2O)_{19}(gly)_2]_n^{2-}$ representing rare examples of structurally characterized amino acid-containing polyoxotungstates.[18,23]

Our ongoing research is focused on the use of lacunary POMs with heteroatoms such as As(III) that possess a stereoactive lone pair of electrons.[16−19] The targeting of these species as building blocks to larger molecules arises from their inability to form closed plenary structures. The lone pair in the precursor helps to direct the self-assembly process, with formation of larger, more complex structures following reaction with electrophiles. Moreover, inclusion of glycine in the present work was anticipated to result in stabilization of novel structures through intramolecular hydrogen-bonding interactions. More specifically, our synthetic approach involves selection of very specific reaction regimes which target the reactivity of the POM precursor, combined with the pH domains that will afford incorporation of glycine and formation of the monoprotonated form of 1,4-diazabicyclooctane (DABCO) as countercation. Inclusion of DABCO as a cation builds upon the use of tertiary ammonium cations that allow a certain degree of control over condensation kinetics.[24]

It was our goal to explore the potential of lacunary polytungstoarsenate(III) ions as ligands for the first POM-supported polynuclear lanthanoid-based SMM. This goal has been achieved through the use of the adaptive polytungstate precursor $[As_2W_{19}O_{67}(H_2O)]^{14-}$.[25] Herein, we report the synthesis, structure, magnetic behavior, and X- and W-band EPR spectroscopy for members of the novel polyoxotungstate family $(HDABCO)_8H_5Li_8[Ln_4As_5W_{40}O_{144}(H_2O)_{10}(Gly)_2]\cdot 25H_2O$, Ln = Gd (**1**), Tb (**2**), Dy (**3**), Ho (**4**), and Y (**5**).

EXPERIMENTAL SECTION

Synthesis. All manipulations were performed under aerobic conditions using materials as received. $Na_2WO_4\cdot 2H_2O$ (Riedel-de Haën >99%), As_2O_3 (Sigma >99%), glycine (Chem-Supply >98.5%), HNO_3, $Gd(NO_3)_3\cdot 6H_2O$ (Aldrich 99.9%), $Tb(NO_3)_3\cdot 5H_2O$ (Aldrich 99.9%), $Dy(NO_3)_3\cdot H_2O$ (Aldrich 99.9%), $Ho(NO_3)_3\cdot 5H_2O$ (Aldrich 99.9%), $Y(NO_3)_3\cdot 6H_2O$, $Li(OAc)\cdot 2H_2O$ (Aldrich reagent grade), and 1,4-diazabicyclooctane (DABCO) (Aldrich >98%). $K_{14}[As_2W_{19}O_{67}(H_2O)]$ was prepared as described previously.[25]

$(HDABCO)_8H_5Li_8[Gd_4As_5W_{40}O_{144}(H_2O)_{10}(gly)_2]\cdot 25H_2O$ (1). A solution of glycine (100 mL, 1.0 M) was acidified to pH 2.05 using 4.0 M HNO_3. To this was added an aqueous 1.0 M solution of $Gd(NO_3)_3\cdot 6H_2O$ (3.6 mL, 3.6 mmol), followed by solid $K_{14}[As_2W_{19}O_{67}(H_2O)]$ (2.95 g, 0.559 mmol). The resulting solution was then heated to 70 °C for 20 min, followed by addition of 4.0 mL of a saturated aqueous solution of DABCO which had been adjusted to pH 2.05 using 4.0 M HNO_3. The resulting precipitate was then collected by filtration. The crude product was suspended in 30 mL of H_2O, followed by addition of 2.0 M LiOAc until the solution became clear. The final pH was 5.7. The clear solution was then left to crystallize in a sealed vial. Rod-shaped, colorless crystals of **1** formed over the course of a few days. The crystals were isolated by filtration and washed with cold 1.0 M glycine (pH 5.7) and the sample air dried. Yield: 1.230 g (37% based on W). Anal. Calcd for **1**, $C_{52}H_{189}As_5Gd_4Li_8N_{18}O_{183}W_{40}$: C, 5.03; H, 1.54; N, 2.03; As, 3.02; Gd, 5.07; Li, 0.45; W 59.27. Found: C, 4.98; H, 1.51; N, 1.96; As, 2.96; Gd, 4.46; Li, 0.35; W, 55.4. Selected IR (KBr, cm^{-1}): 3418 (br), 1628 (m), 1473 (wk), 1412 (wk), 1324 (wk), 1055 (wk), 943 (m), 860 (s), 783 (s), 712 (s), 638 (m), 491 (m).

$(HDABCO)_8H_5Li_8[Ln_4As_5W_{40}O_{144}(H_2O)_{10}(gly)_2]\cdot 25H_2O$ (2−5). Modification of the procedure used to synthesize **1** to obtain the Ln = Tb, Dy, Ho, and Y analogs involved the use of a 1.0 M $Ln(NO_3)_3$ solution of the appropriate rare earth metal. All crystals have the same rod-shaped morphology.

$(HDABCO)_8H_5Li_8[Tb_4As_5W_{40}O_{144}(H_2O)_{10}(gly)_2]\cdot 25H_2O$ (2). Yield: 0.50 g (15% based on W) of rod-shaped colorless crystals. Anal. Calcd for **2**, $C_{52}H_{189}As_5Tb_4Li_8N_{18}O_{183}W_{40}$: C, 5.03; H, 1.53; N, 2.03; As, 3.02; Tb, 5.12; Li, 0.45; W 59.24. Found: C, 5.11; H, 1.63; N, 2.21; As, 2.33; Tb, 4.87; Li, 0.30; W, 59.80. Selected IR (KBr, cm^{-1}): 3417 (br), 1623 (m), 1462 (wk), 1414 (wk), 1323 (wk), 1055 (wk), 946 (m), 852 (s), 781 (s), 707 (s), 635 (m), 477 (m).

dx.doi.org/10.1021/ic200366a |Inorg. Chem. 2011, 50, 7004–7014

Table 1. Crystallographic Data for 1−5

	1	2	3	4	5
formula	$C_{52}H_{189}As_5Gd_4Li_8N_{18}O_{183}W_{40}$	$C_{52}H_{189}As_5Tb_4Li_8N_{18}O_{183}W_{40}$	$C_{52}H_{189}As_5Dy_4Li_8N_{18}O_{183}W_{40}$	$C_{52}H_{189}As_5Ho_4Li_8N_{18}O_{183}W_{40}$	$C_{52}H_{189}As_5Y_4Li_8N_{18}O_{183}W_{40}$
fw, g mol^{-1}	12 408.3	12 415.0	12 429.3	12 439.1	12 134.8
space group	*C*2/*c*	*C*2/*c*	*C*2/*c*	*C*2/*c*	*C*2/*c*
a/Å	28.7051(8)	28.844(4)	28.7245(7)	28.739(4)	28.601(1)
b/Å	25.1709(8)	25.297(7)	25.1124(5)	25.206(4)	25.258(1)
c/Å	35.0928(13)	34.910(6)	35.1823(10)	34.893(5)	35.404(1)
β, deg	110.095(3)	110.042(15)	110.349(3)	110.184(3)	109.599(5)
V/Å^3	23812.2(13)	23930(8)	23794.6(10)	23723(6)	24093(1)
Z	4	4	4	4	4
T/K	130	130	130	130	130
ρ_{calcd}/g cm^{-3}	3.461	3.446	3.470	3.483	3.345
μ/mm^{-1}	43.373	41.803	42.915	21.416	37.109
reflns measd	29 680	21 708	19 828	62 088	25 893
unique reflns	12 587	12 366	7299	20 851	12 384
data/restraints/params	12 587/138/785	12 366/138/776	7299/65/801	20 851/86/1029	12 384/139/776
R_{int}	0.093	0.0775	0.067	0.132	0.097
R_1 [$I > 2\sigma(I)$]	0.072	0.0607	0.043	0.070	0.064
wR_2 (all data)	0.190	0.1756	0.114	0.180	0.174
goodness-of-fit on F^2	0.956	1.147	0.990	0.978	1.016
$\Delta\rho_{max/min}$/e Å^{-3}	3.158, −3.136	2.653, −2.049	1.570, −0.943	3.566, −3.151	3.753, −1.348

$(HDABCO)_8H_5Li_8[Dy_4As_5W_{40}O_{144}(H_2O)_{10}(gly)_2]\cdot 25H_2O$ (3). Yield: 0.60 g (18% based on W) of rod-shaped colorless crystals. Anal. Calcd for **3**, $C_{52}H_{189}As_5Dy_4Li_8N_{18}O_{183}W_{40}$: C, 5.03; H, 1.53; N, 2.03; As, 3.01; Dy, 5.23; Li, 0.45; W 59.17. Found: C, 4.89; H, 1.39; N, 1.78; As, 2.16; Dy, 4.78; W, 57.28. Selected IR (KBr, cm^{-1}): 3417 (br), 1630 (m), 1473 (wk), 1412 (wk), 1324 (wk), 1055 (wk), 942 (m), 859 (s), 785 (s), 711 (s), 636 (m), 478 (m).

$(HDABCO)_8H_5Li_8[Ho_4As_5W_{40}O_{144}(H_2O)_{10}(Gly)_2]\cdot 25H_2O$ (4). Yield: 0.32 g (10% based on W) of rod-shaped pale pink-colored crystals. Anal. Calcd for **4**, $C_{52}H_{189}As_5Ho_4Li_8N_{18}O_{183}W_{40}$: C, 5.02; H, 1.53; N, 2.03; As, 3.01; Ho, 5.30; Li, 0.45; W 59.12. Found: C, 5.05; H, 1.53; N, 2.04; As, 2.25; Ho, 4.97; Li, 0.38; W, 56.24. Selected IR (KBr, cm^{-1}): 3422 (br), 1629 (m), 1473 (wk), 1411 (wk), 1324 (wk), 1055 (wk), 942 (m), 861 (s), 786 (s), 710 (s), 636 (m), 478 (m).

$(HDABCO)_8H_5Li_8[Y_4As_5W_{40}O_{144}(H_2O)_{10}(gly)_2]\cdot 25H_2O$ (5). Yield: 0.30 g (9% based on W) of rod-shaped colorless crystals. Anal. Calcd for **5**, $C_{52}H_{189}As_5Y_4Li_8N_{18}O_{183}W_{40}$: C, 5.15; H, 1.57; N, 2.08; As, 3.09; Y, 2.93; Li, 0.46; W 60.6. Found: C, 5.75; H, 1.76; N, 2.14; As, 2.52; Y, 2.07; Li, 0.37; W 60.2. Selected IR (KBr, cm^{-1}): 3417 (br), 1630 (m), 1473 (wk), 1414 (wk), 1324 (wk), 1055 (wk), 942 (m), 860 (s), 785 (s), 711 (s), 637 (m), 478 (m).

X-ray Data Collection and Structure Solution. The crystallographic data for compounds **1**−**3** and **5** (Table 1) were collected at 130 K on a Gemini Oxford Diffractometer using graphite-monochromated Cu Kα radiation (1.5418 Å). Analytical numerical absorption corrections were carried out using a multifaceted crystal model and the ABSPACK routine within the CrysAlis software package. The data for compound **4** (Table 1) were collected on a Bruker Apex I Diffractometer at 130 K using graphite-monochromatic Mo Kα radiation (0.71073 Å). The structures of **1**−**5** were solved by direct methods and refined by the full-matrix least-squares method on F^2 using the SHELXTL-97 crystallographic package. During the refinement of **1**−**5** a fifth, partially occupied, As(III) center was located on the exterior of the polyanion and initially refined using a free variable. The As(III) refined with between 47% and 52% occupancy for the five structures, so for simplicity the occupancy was fixed to 50% for all five compounds. As is not uncommon for POMs, significant disorder was evident in the solvent water molecules in all of the compounds, which have been refined as fractionally occupied oxygen atoms and have been included in the chemical formula. The number of water molecules of solvation stated in the formula was calculated based on elemental and thermogravimetric analysis. Hydrogen atoms could not be located from the electron density map. Constraints were applied to the atoms of the DABCO molecules to ensure ideal geometry, as they were poorly resolved in the presence of many heavy atoms. Antibumping restraints were also applied to the solvent molecules.

Magnetic Measurements and Modeling. Magnetic susceptibility data were recorded using a Quantum Design MPMS-XL5 SQUID magnetometer for $T = 2.0-290$ K at an applied field of $B_0 = 0.1$ T and at 2.0 K for $B_0 = 0-5$ T. Alternating current (AC) susceptibility measurements were performed for angular frequencies of $\omega = 1-1500$ s^{-1} at $B_0 = 0$ T for $T < 20$ K. The experimental susceptibility values were corrected for the sample holder (cylindrical PTFE capsules) as well as the diamagnetic and temperature-independent paramagnetic (TIP) contributions (derived from compound **1**). Modeling the low-field magnetic direct current (DC) susceptibility data (2−290 K, 0.1 T) for compounds **1**−**4** requires the use an effective, uniform $\{LnO_8\}$ environment that represents both crystallographically independent Ln centers in order to prevent overparametrization. Very weak intramolecular exchange and dipole−dipole coupling between the four Ln^{3+} centers in **1**−**4** are described by an empirical molecular field approach and quantified by the molecular field parameter λ_{mf}, defined as $\chi_m^{-1} = (\chi^{SI}_m)^{-1} + \lambda_{mf}$, where χ^{SI}_m represents the sum of the single-ion contributions of the four Ln^{3+} centers; negative values of λ_{mf} correspond to antiferromagnetic coupling. Our computational framework CONDON was employed to model all DC susceptibility data, and full details are available in the Supporting Information.[26]

EPR Spectroscopy. X-Band EPR spectra were measured with a Bruker Elexsys E500 equipped with a liquid ^{4}He flux cryostat (Oxford Instruments) to work at low temperature. W-Band (ca. 94 GHz) EPR spectra were measured with a Bruker Elexsys E600 CW-spectrometer equipped with a 6 T split-coil superconducting magnet (Oxford Instruments). A Teraflex resonator with a cylindrical cavity was operated

dx.doi.org/10.1021/ic200366a |*Inorg. Chem.* 2011, 50, 7004–7014

in TE_{011} mode. A continuous flow CF935 ^{4}He cryostat by Oxford Instruments was employed for low-temperature work.

Other Measurements. Infrared spectra (KBr disk) were recorded on a Bruker Tensor 27 FTIR spectrometer. C, H, and N analyses were performed at Chemical and Microanalytical Services, Belmont, Australia. Other analyses were carried out by the Microanalytical Unit, Research School of Chemistry, Australian National University; Columbia Analytical, Tucson, AZ; and Zentralabteilung für Chemische Analysen, Research Centre Jülich, Germany.

RESULTS AND DISCUSSION

Syntheses. The synthesis of compounds **1**−**5** was achieved from the reaction of $[As_2W_{19}O_{67}(H_2O)]^{14-}$ in hot acidic glycine solution with nitrate salts of the rare earth metals Gd, Tb, Dy, Ho, and Y in a molar ratio 1:6.44 over a 20 min period. Precipitation of the solid product occurred following addition of a concentrated acidic solution of DABCO at pH = 2.05. The solid was subsequently suspended in 30 mL of water with 2 M lithium acetate solution added dropwise until the solid redissolved, which occurs at approximately pH 5.7. Failure to control the pH within 0.1 of a pH unit results in bulk microcrystalline material of the desired compound (identified by infrared spectroscopy) if the pH is slightly too low (pH range 5.5−5.6) or a significantly decreased yield of crystals of **1**−**5** if the pH is too high (pH range 5.8−6.0). When the synthetic procedure is followed precisely, crystals of **1**−**5** begin to form over the course of 48 h. The synthetic conditions used were carefully selected based on several critical experimental criteria. In particular, it is essential to react the polyanion with the rare earth metal containing glycine solution at pH 2.05, as this ensures a buffered solution due to the glycine carboxylic acid pK_a of 2.34 and good solubility of the $K_{14}[As_2W_{19}O_{67}(H_2O)]$ precursor. The final pH of 5.7 during the formation and crystallization of compounds **1**−**5** appears to lie a little outside the range of 1−4 that has been employed previously for the synthesis of new POMs from the precursor $K_{14}[As_2W_{19}O_{67}(H_2O)]$. This includes $[As_2W_{42}O_{143}(H_2O)_4]^{22-}$, $[As_4W_{19}O_{69}]^{12-}$, and $[As_6W_{65}O_{217}(H_2O)_7]^{26-}$ from other workers[25,27,28] and $[Nd_3As_4W_{41}O_{141}(OH)(H_2O)_{10}]_n^{16-}$, $[Dy_4As_2W_{22}O_{76}(H_2O)_{19}(gly)_2]^{2-}$, $[Tb_4As_2W_{19}O(H_2O)_2(pic)_4]$, and $[Tb_8As_4W_{38}O_{132}(H_2O)_{22}(pic)_{12}]^{12-}$ from our group.[18,19] In all cases the precursor appears to undergo a series of disassembly−reassembly processes that are highly sensitive to variation in reaction conditions, giving rise to compounds that contain recognizable {B-α-AsW_9O_{33}}, {B-β-AsW_9O_{33}}, and {B-β-$AsW_8O_{29}(OH)$} POM subunits held together by other structural components, including extra tungstate fragments that have arisen from partial decomposition of the precursor.[18,19,27−29] The hydrolysis reaction for the formation of the polyanion in compounds **1**−**5** is summarized in eq 1

$$2[As_2W_{19}O_{67}(H_2O)]^{14-} + 4Ln^{3+} + 2WO_4^{2-} + As^{3+} + 2gly + 10H_2O \rightarrow [Ln_4As_5W_{40}O_{144}(gly)_2(H_2O)_{10}]^{21-} + 4H^+ \quad (1)$$

It is clear that in addition to simple structural rearrangement (vide infra), the $[As_2W_{19}O_{67}(H_2O)]^{14-}$ precursor undergoes partial fragmentation to provide the additional As(III) and tungstate components. Excess rare earth metal is also essential for the formation of **1**−**5**, with a reduced rare earth metal content resulting in insoluble products of uncertain composition.

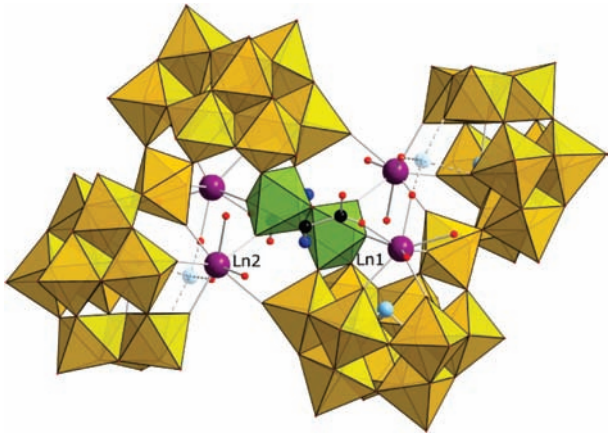

Figure 1. Combined polyhedral/ball-and-stick representation of the isostructural $[Ln_4As_5W_{40}O_{144}(H_2O)_{10}(gly)_2]^{21-}$ polyanions in **1**−**5**. Color code: WO_6 octahedra, yellow/green; Ln/Y, violet; As, pale blue; As (partially occupied), semitransparent blue; C, black; N, dark blue; O, red.

DABCO was selected to provide the countercation due to the pK_a values of 2.97 and 8.82 of its conjugate acids, which are ideal for its controlled protonation/deprotonation and therefore transformation from a dicationic to monocationic species at the pH used for recrystallization of **1**−**5**. This property was exploited by employing lithium acetate to aid the dissolution of the precipitated product, with the presence of lithium dramatically increasing the solubility of the polyanion as the pH is increased. This approach was based on the common practice of improving the solubility of polyoxotungstates for ^{183}W NMR spectroscopy by exchanging the as-synthesized cations for lithium. Furthermore, inclusion of lithium into the reaction mixture is a synthetic strategy that can be exploited to access unique structures by maintaining the dissolution of molecular species that would otherwise be insoluble.[29] Another interesting feature of the recrystallization procedure is that despite the large quantity of acetate in solution, the glycine molecules remain coordinated to the rare earth metal centers with no acetate present in the final crystallized product. This observation suggests that the polyanion is most likely stable in solution, with the added stabilization of the intramolecular hydrogen bonding between the protonated amine of the glycine and the polyanion surface (vide infra) making ligand replacement unfavorable.

Structures. Complete single-crystal X-ray data for compounds **1**−**5** are available in Table 1. The compounds crystallize in the monoclinic space group $C2/c$, with the asymmetric unit containing one-half of the $[Ln_4As_5W_{40}O_{144}(H_2O)_{10}(Gly)_2]^{21-}$ polyanion. Overall, the polyanion (Figure 1) has C_i point symmetry. Selected interatomic distances are provided in Table 2.

The $[As_2W_{19}O_{67}(H_2O)]^{14-}$ heteropolytungstate precursor is composed of two {B-α-$As^{III}W_9O_{33}$} building blocks that are connected by an additional {$WO_5(H_2O)$} fragment, resulting in formation of a vacancy at the center of the cluster with the terminal W═O from the {$WO_5(H_2O)$} directed into the cavity. The cavity is best described as a void between two oxo-rich surfaces. During the synthesis of **1**−**5**, the $[As_2W_{19}O_{67}(H_2O)]^{14-}$ polyanion undergoes a structural rearrangement in order to accommodate inclusion of the Ln^{3+} ions, with conversion into the {$As_2W_{19}O_{68}$} building block. This process occurs via loss of the terminal aqua ligand from the {$WO_5(H_2O)$} linker, with the subsequent change

Table 2. Selected Interatomic Distances (Å) for 1−5

	1	2	3	4	5
Ln1···Ln2	8.163(3)	8.191(3)	8.132(3)	8.144(2)	8.147(4)
Ln1···Ln2′	5.944(3)	5.947(3)	5.908(3)	5.901(2)	5.984(4)
Ln1···Ln1′	9.371(2)	9.384(3)	9.331(3)	9.328(2)	9.445(4)
Ln2···Ln2′	10.776(3)	10.810(3)	10.724(3)	10.738(2)	10.732(4)
Ln1−O(W)	2.33(2)−2.58(2)	2.29(1)−2.59(2)	2.25(2)−2.60(2)	2.27(1)−2.56(2)	2.29(2)−2.57(2)
Ln1−O(H_2O)	2.39(2)−2.54(3)	2.40(2)−2.54(3)	2.40(2)−2.52(2)	2.32(2)−2.49(2)	2.37(2)−2.51(3)
Ln1−O34	2.41(3)	2.37(2)	2.33(3)	2.29(2)	2.38(3)
Ln2−O(W)	2.30(2)−2.40(2)	2.29(2)−2.34(2)	2.27(2)−2.37(2)	2.25(2)−2.36(2)	2.30(2)−2.36(2)
Ln2−O78	2.31(3)	2.34(2)	2.27(3)	2.31(2)	2.32(3)
Ln2−O(H_2O)	2.40(2)−2.52(3)	2.40(3)−2.54(2)	2.39(3)−2.45(2)	2.31(2)−2.49(2)	2.39(3)−2.47(2)
Ln2−O36	2.41(3)	2.38(2)	2.39(2)	2.34(2)	2.35(3)
As3/vacancy−O34	1.79(3)	1.87(2)	1.81(3)	1.87(2)	1.83(3)
As3/vacancy−O36	1.79(3)	1.83(2)	1.73(2)	1.84(2)	1.85(3)
W−O(Ln1)	1.74(2)−1.79(2)	1.73(2)−1.77(1)	1.72(2)−1.71(2)	1.74(2)−1.78(2)	1.75(2)−1.81(2)
W−O(Ln2)	1.73(2)−1.83(2)	1.75(2)−1.81(2)	1.76(2)−1.77(2)	1.76(2)−1.82(2)	1.76(2)−1.81(2)
N1···O35[a]	2.99(3)	3.00(3)	3.00(3)	2.99(3)	3.04((3)
N1···O48[a]	2.76(4)	2.81(4)	2.74(3)	2.77(4)	2.91(3)
N1···O77[a]	2.76(3)	2.79(3)	2.78(4)	2.79(3)	2.82(3)
N2···O35[b]	2.62(3)	2.59(3)	2.61(3)	2.63(2)	2.58(3)
N3···O(W)[b]	2.87(3)−3.38(3)	2.89(3)−3.39(3)	2.89(4)−3.38(5)	2.85(3)−3.40(3)	2.87(3)−3.38(3)
N4···O7[b]	2.83(3)	2.80(2)	2.79(3)	2.81(2)	2.77(3)
N5···O(W)[b]	2.88(3)−3.29(3)	2.91(3)−3.35(3)	2.88(4)−3.30(4)	2.87(3)−3.35(2)	2.84(3)−3.32(3)

[a] Intramolecular N−H···O bonds. [b] Intermolecular N−H···O bonds.

in the respective orientation of the two trivacant {B-α-AsW_9O_{33}} units (Figure 2). Consequently, the size of the cavity and geometry of the coordination sites that the lacunary polyanion presents to the electrophilic rare earth metal ions are altered, allowing the coordination modes observed in the $[Ln_4As_5W_{40}O_{144}(H_2O)_{10}(gly)_2]^{21-}$ polyanions of **1**−**5**. The rearranged {$As_2W_{19}O_{68}$} subunit found in **1**−**5** has been observed previously as a building block of complexes $[Yb_{10}As_{10}W_{88}O_{308}(OH)_8(H_2O)_{28}(OAc)_4]^{40-}$ and $[Nd_3As_4W_{41}O_{141}(OH)(H_2O)_{10}]_n^{16-}$.[16,18] Bond valence sum calculations indicate no well-defined localized protonation of the polyanion surface.[30]

The polyanions of compounds **1**−**5** are composed of two {$As_2W_{19}O_{68}$} units, which are cross-linked through two symmetry equivalent W−O−Ln connections and an edge-shared dioxo-bridged ditungsten unit which is located on the molecular inversion center. Each of the two unique rare earth metal centers is eight coordinate, and careful inspection of the bond angles suggests that the coordination geometry is best described as distorted square antiprismatic. Rare earth metal center Ln1 coordinates to five terminal oxo sites of the POM framework with four shorter Ln−O(W) bonds and one longer bond to the other half of the polyanion (Table 2). Metal center Ln1 binds to two terminal aqua ligands and a fully occupied oxo ligand, which has been refined as belonging to a partially occupied {$As^{III}O_4$} unit with approximate "seesaw" coordination geometry (sp^3d hybridized to give a trigonal bipyramidal electron pair geometry with a stereoactive lone pair of electrons in an equatorial position). This oxygen position has therefore been interpreted as a μ_2-bridging oxo in the presence of arsenic at this site and as a terminal aqua ligand in the absence of the arsenic atom. A similar peripheral {$As^{III}O_4$} unit has been observed previously in the polyoxomolybdate $[As_2Mo_8V_4AsO_{40}]^{5-}$.[31] The second crystallographically unique

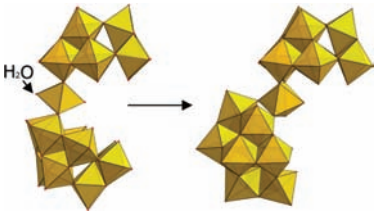

Figure 2. Polyhedral representation of the {As_2W_{19}} transformation from the precursor $[As_2W_{19}O_{67}(H_2O)]^{14-}$ (left) to the {$As_2W_{19}O_{68}$}$^{16-}$ fragment of **1**−**5** (right).

rare earth metal center, Ln2, coordinates to the POM through four Ln−(μ_2O)−W linkages, which fill one of the basal coordination planes of the rare earth metal. Additionally, Ln2 also coordinates to a partially occupied {$As^{III}O_4$} unit, with terminal aqua ligands bound to the rare earth metal center when the arsenic site is vacant. The three remaining coordination sites are occupied by two terminal aqua ligands and a zwitterionic glycine through monodentate coordination to the carboxylate functional group. The pH of 5.7 at which **1**−**5** crystallize, ensures the cationic nature of the glycine amine group (pK_a = 9.78). Incorporation of glycine represents a rare example of amino acid inclusion within a polyoxotungstate, with other examples including coordination of glycine or alanine through the carboxylate functional group via terminal or bridging binding modes to both lanthanoid and tungsten metal centers.[18,23] A notable feature of amino acid ligands in comparison to simple carboxylates is the additional structural stabilization provided by intramolecular hydrogen bonding of the protonated amine to oxo ligands of the POM framework and in this case also to an aqua ligand from the other rare earth center (Figure 3, Table 2). The hydrogen atoms could not be located crystallographically.

dx.doi.org/10.1021/ic200366a |*Inorg. Chem.* 2011, 50, 7004–7014

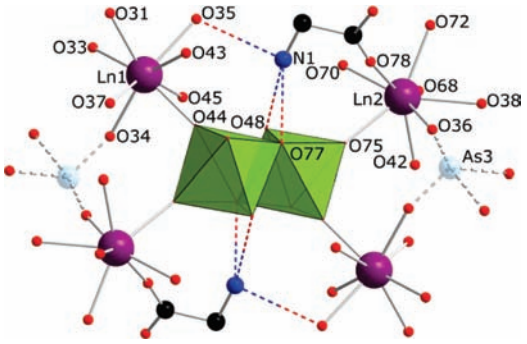

Figure 3. Combined polyhedral/ball-and-stick representation of the central core of **1**−**5**. The intramolecular hydrogen bonds between the protonated amine and the terminal oxo ligands of the ditungsten unit and the aqua ligands of the Ln linker are shown as broken blue-red lines. Color code as in Figure 1.

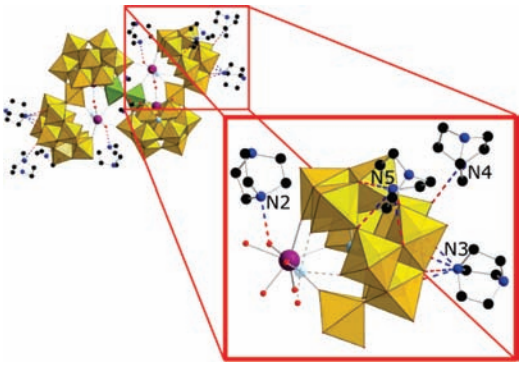

Figure 4. Graphical representation of the hydrogen bonding between the eight HDABCO countercations and the $[Ln_4As_5W_{40}O_{144}(H_2O)_{10}(gly)_2]^{21-}$ polyanion in **1**−**5**.

Table 3. Structural Parameters Related to the Ln Coordination Spheres in 1−5

compound	Ln	Ln(3+) radius[a] (Å)	d_{in}[b] (Å)	d_{pp}[c] (Å)	ϕ[d] (deg)	ψ[e] (deg)
1	Gd1	1.053	2.859	2.616	43.69	6.638
	Gd2		2.841	2.565	42.20	2.220
2	Tb1	1.040	2.864	2.629	43.344	5.197
	Tb2		2.824	2.558	42.013	0.946
3	Dy1	1.027	2.866	2.601	42.83	7.107
	Dy2		2.781	2.544	43.07	1.883
4	Ho1	1.015	2.806	2.586	43.67	5.914
	Ho2		2.784	2.526	42.82	1.590
5	Y1	1.019	2.857	2.587	41.13	6.758
	Y2		2.805	2.544	42.17	1.126

[a] From ref 32. [b] Intraplanar distance. [c] Interplanar distance. [d] Skew angle. [e] Angle between normal vectors of oxygen-based square planes.

The dependence of the magnetic behavior of lanthanoid complexes on both strength and symmetry of the ligand field (vide infra) acting on the lanthanoid centers renders a closer examination of the coordination environment of the individual lanthanoid centers of interest. The polyanions in compounds **1**−**5** each possess two independent Ln centers that both display distorted square antiprismatic coordination geometry, giving rise to approximate D_{4d} local site symmetry. The two square planes for Ln1 are defined by the oxygen atoms O35, O43, O44, O45 and O31, O33, O34, O37, while for Ln2 they are defined by the oxygen atoms O36, O38, O72, O78 and O42, O68, O70, O75 (Figure S1, Supporting Information). It should be emphasized that these two planes are not strictly coplanar, with the angle between their normal vectors (ψ) significantly larger for Ln1 than for Ln2 in each case (Table 3). The intraplanar distances (d_{in}), calculated as the average distance between the four neighboring oxygen atoms in each plane, the interplanar distances (d_{pp}), calculated as the distance between the upper and lower planes defined by the four oxygen atoms, and the skew angles (ϕ), calculated as the offset between the two square planes defined by the mean planes through the coordinating oxygen atoms are also provided in Table 3. Significant axial compression is observed for both the rare earth centers in the five complexes, with d_{in} larger than d_{pp} in all cases, while the skew angles are close to the 45° expected for ideal D_{4d} point symmetry. In addition, the angles between the C_4 axes of Ln1 and Ln2 centers in compounds **1**−**5** are in the range 81.5−81.7°.

Intermolecular Interactions and Crystal Packing. Stabilization of the polyanions in the crystal lattice of **1**−**5** is increased via extensive intermolecular hydrogen bonding between multiple HDABCO cations and the oxygen-rich surface of the polyanion. These interactions are highlighted in Figure 4, with the proton associated with the amine of two HDABCO counterions oriented directly toward two of the small cavities between the $\{W_3O_{13}\}$ triads within the $\{AsW_9O_{33}\}$ subunits. Each of the protonated amines form four hydrogen bonds to the polyanion through the corner-sharing μ_2-O ligands which form the edges of the square faces that are located between the $\{W_3O_{13}\}$ triads in the $\{AsW_9O_{33}\}$ portions of the polyanion (Figure 4 and Table 2). Hydrogen-bond donation also exists from the protonated amine of HDABCO to a terminal oxo of the polyanion. Crystallographic evidence that the HDABCO counterions exist in the monocationic form is supported by the observation of hydrogen bonding between the terminal aqua ligand on Ln1 and the basic tertiary amine of the organic counterion. Further extensive hydrogen-bonding interactions are observed throughout the crystal lattice, including multiple HDABCO−solvent interactions.

Other notable features of the crystal packing are the AA, AA, and AB arrangement of the polyanions along the crystallographic *a*, *b*, and *c* axes, respectively (Figure S2, Supporting Information). This results in two different orientations of the POM molecules in the crystal lattice, with angles between the normals of the molecular Ln_4 planes in the range 62−63° for **1**−**5**. Intermolecular separations, defined as nearest neighbor inversion center to inversion center distances, are 19.1 Å for the five compounds, while the closest intermolecular W···W separations are 6.4 Å in each case.

Infrared Spectroscopy. The infrared spectra of compounds **1**−**5** are all very similar with only slight shifts in the position of the bands (Figure S3, Supporting Information). All compounds show broad peaks at 3400 and 1623 cm^{-1} which are attributed to the stretching and bending modes of lattice and coordinated water molecules. A characteristic peak for the polyanion at 946 cm^{-1} can be assigned to the W═O stretching vibration, peaks at 852 and 790 cm^{-1} correspond to the two types of W−O−W stretching vibrations, and the peak at 707 cm^{-1} can be assigned to the W−O(−As) stretch.[33] A sharp band of weak to moderate intensity at 1055 cm^{-1} is likely due to an As−O stretch

dx.doi.org/10.1021/ic200366a |*Inorg. Chem.* 2011, 50, 7004–7014

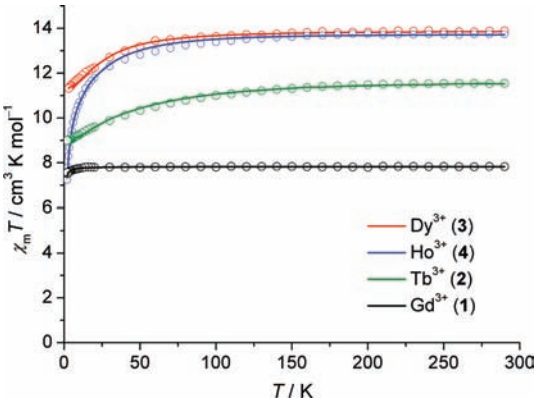

Figure 5. Temperature dependence of $\chi_m T$ for four members of the $(HDABCO)_8H_5Li_8[Ln_4As_5W_{40}O_{144}(H_2O)_{10}(Gly)_2]\cdot 25H_2O$ family (Ln = Gd, Tb, Dy, and Ho), referenced to a single Ln center. The solid lines are least-squares fits as described in the text.

of the peripheral $\{As^{III}O_4\}$ unit.[34] The band at 1630 cm^{-1} is assigned to COO stretching vibrations from the carboxylate of the monodentate-coordinated glycine molecules.[35]

Direct Current Magnetic Susceptibility. The variable-temperature magnetic susceptibility data (applied magnetic field $B_0 = 0.1$ T) for compound **1** with four Gd^{3+} centers ($4f^7$, $^8S_{7/2}$) reveal spin-only magnetic behavior (Figure 5). A nearly perfect Curie-type susceptibility plot results with temperature-independent $\chi_m T$ behavior ($C = 7.825$ cm^3 K mol^{-1} for a spin-only Gd^{3+} free ion). The corresponding value per Gd^{3+} site amounts to 7.87 cm^3 K mol^{-1} with an isotropic g value of 1.993. The magnetization as a function of external static field shows Brillouin-type behavior (Figure S4, Supporting Information). The model Hamiltonian utilizes a common ligand field, characterized by standard Slater−Condon parameters ($^2F = 91\,800$ cm^{-1}, $^4F = 64\,425$ cm^{-1}, $^6F = 49\,258$ cm^{-1}) and standard spin−orbit coupling constant ($\zeta = 1470$ cm^{-1}).[36] Note that the reduced g value of 1.993 is a result of the large spin−orbit interaction that mixes significant amounts of other terms into the $J = 7/2$ ground state. The major Russell−Saunders components of the ground state are ^8S (97%) and ^6P (2.7%), affording a g_J factor of 1.993.[37] The slight decrease of $\chi_m T$ below 8.0 K is predominantly due to a saturation effect and not associated with antiferromagnetic exchange interactions between the four Gd^{3+} centers.

For the Tb^{3+}-based compound **2** ($4f^8$, $^7F_6$), the Dy^{3+}-based compound **3** ($4f^9$, $^6H_{15/2}$), and the Ho^{3+}-based compound **4** ($4f^{10}$, $5I_8$), the approximately D_{4d}-symmetric, square antiprismatic ligand field causes a splitting of the J ground state into M_J sublevels and an energetic separation between the lowest and the higher M_J states due to both ligand field effects and spin−orbit coupling. For all three compounds, the observed increase in $\chi_m T$ with increasing temperatures reflects increasing thermal population of higher multiplet states and is, again, of single-ion origin (Figure 5). At 290 K compound **2** reaches a $\chi_m T$ value of 11.5 cm^3 K mol^{-1} per Tb^{3+} ion, close to the corresponding value of 11.82 cm^3 K mol^{-1} for the free-ion approximation ($\chi_m T = N_A\mu_B{}^2 g_J J(J+1)/3k_B$). Compound **3** approaches a room-temperature $\chi_m T$ value of 13.9 cm^3 K mol^{-1}, in good agreement with the corresponding value of 14.17 cm^3 K mol^{-1} for a free Dy^{3+} ion. Correspondingly, compound **4** approaches 13.7 cm^3 K mol^{-1} at room temperature, slightly below the free-ion value of 14.07 cm^3 K mol^{-1}.

Modeling the magnetic characteristics of compounds **2**−**4** requires accounting for the interelectronic repulsion (H_{ee}), spin−orbit coupling (H_{so}), and ligand field effects (H_{lf}). We note that the correct description of the ligand field represents a challenge. To reduce the number of independent ligand field fitting parameters, the two distinct Ln^{3+} sites were treated as single average environment, the point symmetry of which was idealized from C_s to D_{4d}. The angles ϕ for compounds **2**−**4** (see Table 3) correspond approximately to the expected angle for an ideal D_{4d} symmetry ($\phi = 45°$). In this ideal case, $B^k{}_q$ values with $q \neq 0$ ($B^4{}_4$ and $B^6{}_4$) would be exactly zero. Further, model calculations show that small values of these parameters, as expected for small deviations from ideal symmetry, have an insignificant effect on the magnetic data. Thus, the effective Hamiltonian for the ligand field modulation is given by

$$H_{lf} = B^2_0 \sum_{i=1}^{N} C^2_0(i) + B^4_0 \sum_{i=1}^{N} C^4_0(i) + B^6_0 \sum_{i=1}^{N} C^6_0(i) \qquad (2)$$

Initial sets of $B^k{}_q$ parameter values (Wybourne notation) from spectroscopically determined energy levels for Ln^{3+} compounds with D_{4h} symmetry were used in the fitting procedure.[38] The signs of the ligand field parameters are fixed and assigned from separate point charge electrostatic model calculations, which are based on the exact $\{LnO_8\}$ geometries; the negative values of $B^2{}_0$ and $B^4{}_0$ and the positive ones for $B^6{}_0$ correspond to the point charge model for an axially compressed square antiprismatic (D_{4d}) ligand field. In order to determine the interdependent ligand field parameters $B^k{}_q$ the assumption of D_{4d} symmetry yields excellent fits (Figure 5) with the derived $B^2{}_0$, $B^4{}_0$, and $B^6{}_0$ values listed in Table 4. Note the corresponding continuous trends in $B^2{}_0$, $B^4{}_0$, and $B^6{}_0$ going from Tb^{3+} to Dy^{3+} to Ho^{3+}, as expected from the increase in effective nuclear charge (Z_{eff}) of these ions. It is notable that both the signs of the three parameters and the trends observed with increasing Z_{eff} are the same as those determined for the equivalent parameters in the $[Ln(\beta_2\text{-}SiW_{11}O_{39})_2]^{13-}$ family of compounds.[8] In contrast, the $B^2{}_0$ parameters are of opposite sign to those determined for the $[Pc_2Ln]^-$ family (with negligible axial distortion),[12] and the trend in $B^k{}_q$ parameters is opposite to that observed for the

Table 4. Spin Hamiltonian Parameters Used for and Derived from Magnetochemical Modeling of the $(HDABCO)_8H_5Li_8[Ln_4As_5W_{40}O_{144}(H_2O)_{10}(gly)_2]\cdot 25H_2O$ family

parameters	1	2	3	4
Ln^{3+}	Gd^{3+}	Tb^{3+}	Dy^{3+}	Ho^{3+}
electron configuration	$4f^7$	$4f^8$	$4f^9$	$4f^{10}$
ground term	$^8S_{7/2}$	$^7F_6$	$^6H_{15/2}$	$^4I_8$
F^2/cm^{-1}	91 800	97 650	94 500	101 250
F^4/cm^{-1}	64 425	68 530	66 320	71 057
F^6/cm^{-1}	49 258	52 397	50 706	54 328
ζ/cm^{-1}	1470	1705	1900	2160
$B^2{}_0$/cm^{-1}		−25	−340	−480
$B^4{}_0$/cm^{-1}		−1510	−1425	−1375
$B^6{}_0$/cm^{-1}		155	205	225
$\lambda_{mf}/10^3$ mol cm^{-3}		−27.64	−10.12	−5.65
LFSO[a]/cm^{-1}		244	345	211
SQ[b]	0.5%	1.3%	1.6%	1.9%

[a] Overall ligand field splitting. [b] $SQ = (FQ)^{1/2}$, where $FQ = \Sigma_{i=1}{}^n([\chi_{obs}(i) - \chi_{calc}(i)]/\chi_{obs}(i))^2$.

dx.doi.org/10.1021/ic200366a |Inorg. Chem. 2011, 50, 7004–7014

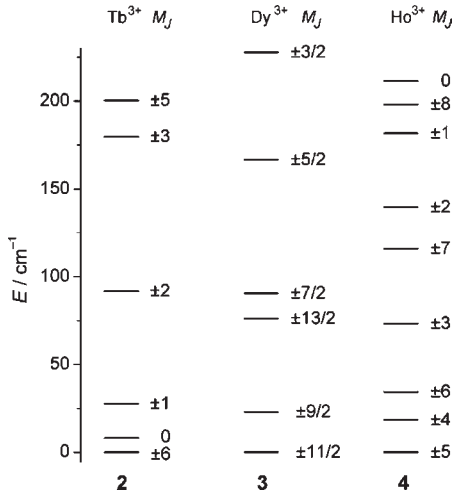

Figure 6. Energy level diagrams of the ground-state multiplets for compounds **2**, **3**, and **4**. Not shown are M_J sublevels above 230 cm^{-1} (for **2**, $M_J = \pm 4$ at 244.4 cm^{-1}; for **3**, $M_J = \pm 1/2$ at 261.1 cm^{-1} and $M_J = \pm 15/2$ at 344.5 cm^{-1}).

$[Ln(W_5O_{18})]^{9-}$ family,[8] while the signs of, and trends in, the other parameters are the same.

For **2**−**4**, the energies of the M_J sublevels are determined by the ligand field parameters derived from the least-squares fits (Figure 6, Table S1, Supporting Information). We find that the exact splitting of the M_J sublevels for the Tb^{3+} sites in **2** is rather sensitive to variations in B^k_q values, and our fits indicate the energetically lowest substates to be $M_J = \pm 6$ (with a first excited $M_J = 0$ lying only 8 cm^{-1} above in energy). The lowest substate level for the Dy^{3+} sites in **3** results as $M_J = \pm 11/2$, and for the Ho^{3+} sites in **4** it is $M_J = \pm 5$ (with first excited $M_J = \pm 9/2$ and $M_J = \pm 4$ lying, respectively, 23 and 18 cm^{-1} above in energy). Overall, the derived energy level diagrams for **2**−**4** are broadly similar to those derived for the $[Ln(W_5O_{18})]^{9-}$ and $[Ln(\beta_2\text{-}SiW_{11}O_{39})_2]^{13-}$ structural families,[8] although the precise ordering of the M_J sublevels and the actual energies differ. We note that the calculated overall ligand field splittings (Table 4) are smaller than corresponding values determined for lanthanoid complexes with less symmetric (e.g., C_2) ligand field environments.[39]

Alternating Current Magnetic Susceptibility. As compounds **2**−**4** exhibit energy separations between the energetically lowest M_J sublevels (Figure 6), possibly resulting in a slowing down of the phonon-mediated magnetization relaxation at low temperatures and concurrent hysteretic behavior, frequency-dependent alternating current (AC) susceptibility measurements were performed for T = 2−10 K and angular frequencies of 1−1500 Hz in the absence of a DC bias field (a 10 G DC bias field does not significantly change the AC susceptibility values). While no significant out-of-phase susceptibility component (χ_m'') down to 2.0 K is observed for the Tb^{3+} and Ho^{3+} compounds **2** and **4**, the Dy^{3+} compound **3** exhibits frequency-dependent in-phase and out-of-phase components characteristic of SMMs (Figure S4, Supporting Information). However, the standard procedure established for SMMs to derive the effective energy barrier between the lowest M_J states cannot be used for **3** as χ_m'' does not reach clearly defined maxima down to 2.0 K (Figure 7). In the absence of such maxima, the out-of-phase susceptibility data below 3.6 K were therefore fitted by a generalized Debye model,[40] which allows determination of the

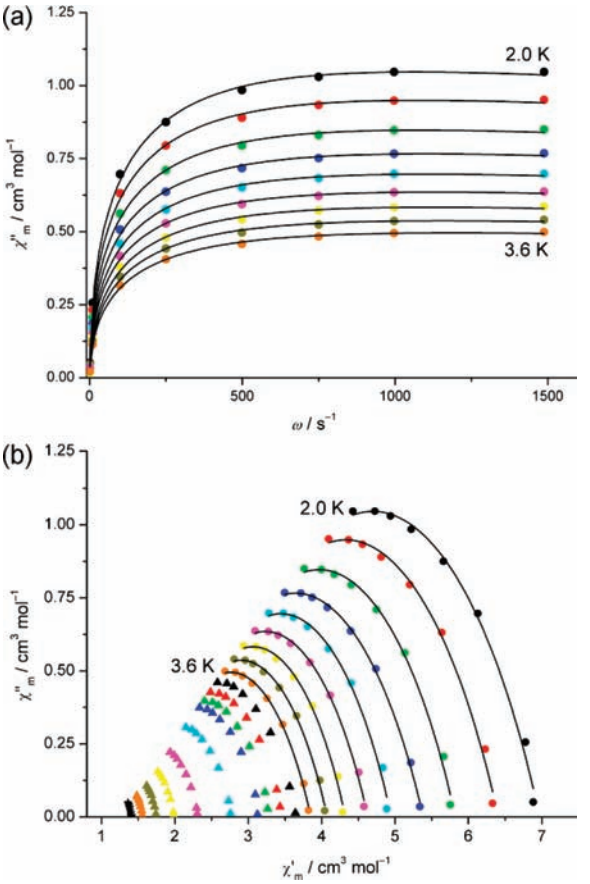

Figure 7. Low-temperature AC susceptibility data for **3**. (a) Frequency dependence of the out-of-phase ac component χ_M'' for **3** from 2.0 to 3.6 K in intervals of 0.2 K. (b) Cole−Cole plot (χ_m'' vs χ_m') from 2.0 to 10.0 K. Symbols, experimental data; black graphs, least-squares fits to a Debye model. Note that adequate fits are only obtained up to 3.6 K.

average relaxation times of the magnetization, τ, for each temperature. The temperature dependence of τ is fitted to an Arrhenius expression, $\tau = \tau_0 \exp(\Delta_{eff}/k_BT)$, which yields an effective barrier $\Delta_{eff} = 3.9(1)$ K and $\tau_0 = 1.9 \times 10^{-5}$ s (Figure S5, Supporting Information). The distribution width of τ is quantified by the scalar parameter α in the Debye model (α = 0−1, with 0 for a single relaxation time and 1 for an infinitely broad distribution) and here amounts to 0.45, i.e., indicating the presence of multiple relaxation times due to multiple relaxation mechanisms. This is consistent with the presence of two crystallographically distinct Dy^{3+} ligand environments giving rise to different magnetization relaxation processes.

Electron Paramagnetic Resonance Spectroscopy. The low-temperature X-band EPR spectrum of **1** (Figure S6, Supporting Information) shows clear signs of fine structure at low field (0−100 mT) with effective g values of 13.7 and 6.7 and a very broad feature centered at g = 2.32 (B = 290 mT) and extending up to 1 T. Such a broad spectrum is different from those reported in the literature for Gd-containing POM systems,[41] characterized by well-defined fine structure, and suggests that even if weak and undetectable by magnetic measurements, spin−spin interaction between adjacent Gd^{3+} centers is not negligible in the interpretation of the spectrum. To obtain more information concerning the anisotropy and symmetry of the ligand field environment of the Gd^{3+} centers, we then

dx.doi.org/10.1021/ic200366a |Inorg. Chem. 2011, 50, 7004–7014

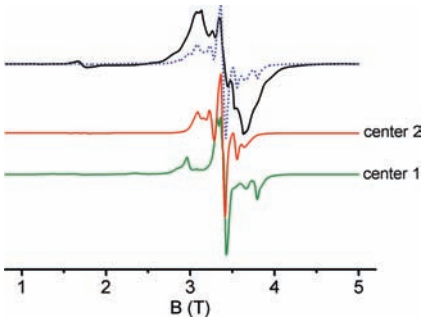

Figure 8. Experimental W-band (94.1025 GHz) EPR spectrum of **1** measured at 15 K (solid black line), and simulation obtained busing the spin Hamiltonian parameters reported in the text (dotted blue line). The individual simulated spectra of the two Gd^{3+} centers are presented as solid green and red lines.

decided to perform W-band (ca. 94 GHz) EPR spectroscopy. These higher field measurements should ideally provide better resolution of the fine structure of the system associated with ligand field splitting and allow discrimination between signals arising from the two crystallographically independent centers. High-field EPR spectroscopy has indeed previously been reported to be particularly well suited for providing detailed information about the zero-field splitting (ZFS) of Gd^{3+} ions in different symmetry environments.[42] The spectrum observed at 15 K (Figure 8) is dominated by a structured band centered around $g = 2.00$ and shows a prominent transition at half field. To obtain some quantitative information about the ZFS parameters, complete simulations of the spectrum would be needed. However, even after neglecting the supposedly weak effects of the exchange interactions between Gd^{3+} centers and assuming idealized tetragonal (D_{4h}) point symmetry the following spin Hamiltonian for each of the crystallographically independent spin centers has to be considered

$$\hat{\mathbf{H}}_{\mathrm{EPR}} = \mu_{\mathrm{B}}\mathbf{S}\cdot\mathbf{g}\cdot\mathbf{B} + D\hat{S}_z^{\,2} + B_{40}\hat{\mathbf{O}}_4^0 + B_{44}\hat{\mathbf{O}}_4^4 + B_{60}\hat{\mathbf{O}}_6^0 + B_{64}\hat{\mathbf{O}}_6^4 \quad (3)$$

where B_{kq} are the Stevens spin Hamiltonian parameters (not to be confused with the Wybourne ligand field ones of Hamiltonian (2)) and $\hat{\mathbf{O}}_{\mathrm{k}}^{\mathrm{q}}$ the corresponding equivalent operators.[43]

It is evident that even by neglecting sixth-order terms in the simulation process, the number of parameters to be varied is quite large and the spectrum too complex to obtain a perfect simulation. At any rate, sample simulations showed that in order to obtain a reasonable reproduction of the experimental features (Figure 8) it has to be assumed that the two crystallographically different Gd^{3+} centers are characterized by quite different spin Hamiltonian parameters (at least in relative terms), indicating a strong sensitivity of EPR parameters to relatively small differences in the coordination sphere. Accordingly, the best reproduction was obtained by assuming a 1:1 ratio for the two centers and the following parameter values: $g_{\mathrm{iso}}^{(1,2)} = 1.993 \pm 0.002$, $|D^{(1)}| = 0.06 \pm 0.02\ \mathrm{cm}^{-1}$, $|D^{(2)}| = 0.09 \pm 0.02\ \mathrm{cm}^{-1}$, $B_{40}^{(1)} = 2.0 \pm 1.0 \times 10^{-4}\ \mathrm{cm}^{-1}$, $B_{40}^{(2)} = 3.0 \pm 1.0 \times 10^{-4}\ \mathrm{cm}^{-1}$, $B_{44}^{(1)} = 4.5 \pm 1.0 \times 10^{-3}\ \mathrm{cm}^{-1}$, $B_{44}^{(2)} = 0.9 \pm 0.2 \times 10^{-3}\ \mathrm{cm}^{-1}$, where (1) and (2) refer to the two crystallographically independent Gd^{3+} centers and the large relative uncertainties on the parameter values reflect the large correlation between them and the less than perfect quality of the simulation.

Indeed, while most of the spectral features are reproduced in terms of transition fields, the corresponding line shapes and relative intensities of the lines are not completely satisfactory. This may be due to the neglect of the low-symmetry components in the spin Hamiltonian induced by assumption of idealized tetragonal symmetry (whereas each center actually experiences C_i point symmetry) and/or of the sixth-order terms. Finally, it has to be considered that even an exchange interaction of magnitude much smaller than that detectable by magnetic measurements may affect the quality of the simulations, with a likely particular impact on the intensity of the half field transition, currently underestimated by the simulation.

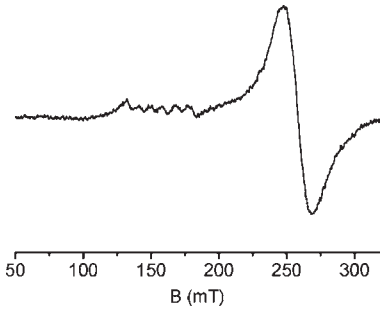

Figure 9. X-band EPR spectrum of **3** observed at 40 K.

A comparison of the obtained ZFS parameters with literature data reveals that the values of the D parameter are, on average, twice as large compared to those reported for tungstosilicate and tungstophosphate Gd-containing POMs.[44] We tentatively assign this result to the quite relevant axial compression of the coordination environment of Gd^{3+} centers (vide supra). Also, the values of B_{44} parameters are quite large, indicating a considerable deviation of the coordination geometry from ideal D_{4d} (for which they should be zero). The ability of EPR spectroscopy to determine these terms, in contrast to powder magnetic measurements, which are largely insensitive to them, is of particular importance, since transverse terms mix states with different M_J values and may thus affect the low-temperature magnetization dynamics of these systems by allowing relaxation by a tunneling mechanism.

To address this point in more detail, the low-temperature X-band EPR spectrum of **3** was recorded (Figure 9). EPR spectra of Kramers lanthanoids metal ions are usually analyzed in terms of an effective spin Hamiltonian, considering that only one doublet of the ground J multiplet is populated. This is treated as an effective $S = 1/2$ system, which then gives rise to a very anisotropic g pattern, with $g_{\parallel} \neq g_{\perp} \neq g_e$. The values of $g_{\parallel}$ and $g_{\perp}$ are related to the composition of the EPR-active doublet wave function in terms of the different M_J states. In this framework, the EPR spectrum of **3** is easily interpreted as arising from $S_{\mathrm{eff}} = 1/2$, with $g_{\parallel} = 4.4$ and $g_{\perp} = 2.67$. In the parallel region the hyperfine splitting due to the $I = 5/2$ nuclei of the ^{161}Dy and ^{163}Dy isotopes is also observed, with $A_{\parallel} = 85$ G.

The signal intensities are strongly temperature dependent, showing a maximum at around 40 K and disappearing below 20 K. This suggests that the EPR-active substate is $M_J = \pm 9/2$, which according to ligand field calculations lies 23 cm^{-1} (i.e., 34 K) above the ground state. However, observation of an EPR spectrum with $g_{\perp} \neq 0$ indicates that the transverse fourth-order ligand field components are different from zero, since these terms provide the only means to observe a nonzero perpendicular component of the spectrum. Indeed, the EPR-active doublet would then be

$$|\pm\Gamma\rangle = a|\pm 9/2\rangle + b|\pm 1/2\rangle + c|\mp 7/2\rangle \quad (4)$$

dx.doi.org/10.1021/ic200366a |*Inorg. Chem.* 2011, 50, 7004–7014

with corresponding effective g values

$$g_{\perp} = 2g_J(4b^2 + 4\sqrt{3}ac) \quad (5a)$$

$$g_{\parallel} = g_J(9a^2 + b^2 - 7c^2) \quad (5b)$$

This would suggest a rather large mixing induced by fourth-order terms, since the condition $a^2 + b^2 + c^2 = 1$ implies either $a^2 = 0.370$, $b^2 = 0.550$, $c^2 = 0.08$ (for $g_{\perp} > 0$) or $a^2 = 0.50$, $b^2 = 0.30$, $c^2 = 0.20$ (for $g_{\perp} < 0$)[40] to justify the observed results. On the other hand, the absence of a signal from the ground doublet has probably to be attributed to an EPR transition probability too weak to observe a signal. In this respect, we recall here that the observation of an EPR signal from an excited doublet of a Dy^{3+} center has been previously reported by Baker and Bleaney for the ethylsulphate salt,[45] the ground doublet of which is also EPR silent.

Finally, we note that no apparent difference is observed between the two crystallographically independent Dy^{3+} centers. This is not in contradiction with the observation for **1**, as it reflects the weak effect of a small difference in the ligand field splitting on the effective g values, which are mainly related to the eigenvectors of the EPR-active doublet. On the contrary, for Gd^{3+}, a difference in the ligand field splitting is directly reflected in the ZFS parameters of the corresponding spin Hamiltonian, especially in the higher order terms.

Origin of Slow Magnetic Relaxation. Of the compounds described herein, only the Dy-containing species, **3**, displays slow magnetic relaxation above 2.0 K, although it is possible that some of the other analogs may manifest slow magnetic relaxation at lower temperatures. It is informative to compare this behavior with that reported by Coronado et al. for the two POM-supported mononuclear lanthanoid-based SMM families $[Ln(W_5O_{18})_2]^{9-}$ (Ln = Ho and Er) and $[Ln(\beta_2\text{-}SiW_{11}O_{39})_2]^{13-}$ (Ln = Dy, Ho, Er and Yb).[8] In the detailed study of these two structural families, the members that display slow magnetic relaxation all manifest Ising-type magnetic anisotropy characterized by lowest energy sublevels with relatively large $|M_J|$ values, with the sublevels with small $|M_J|$ values lying at higher energy. In the present study, this situation exists for both Dy and Ho analogs **3** and **4**, with a lowest energy sublevel with $M_J = \pm 11/2$ within the $J = 15/2$ ground state for **3**, whereas for **4** the lowest energy sublevel has $M_J = \pm 5$ within the $J = 8$ ground state. For the Tb-containing species **2**, although the $M_J = \pm 6$ is the lowest energy sublevel within the $J = 6$ ground state, only 8.1 cm^{-1} above lies the next highest energy level, characterized by $M_J = 0$. Of course the situation for **2**−**4** is complicated by the presence of two different lanthanoid environments, whereas only one such environment is present in $[Ln(W_5O_{18})_2]^{9-}$ and $[Ln(\beta_2\text{-}SiW_{11}O_{39})_2]^{13-}$. Thus, the ligand field parameters and resulting energy levels derived in the present study can only represent an average for the two sites. In the study by Coronado et al. the $[Ln(W_5O_{18})_2]^{9-}$ family of SMMs displayed slow magnetic relaxation at higher temperatures than the $[Ln(\beta_2\text{-}SiW_{11}O_{39})_2]^{13-}$ family, despite the similar pattern in the energies of the M_J substates for members of the two families containing the same lanthanoid ion. From careful analysis of the structural parameters associated with the local lanthanoid coordination environment it was apparent that although axially compressed approximate D_{4d} local site symmetry was evident in both families, a deviation from strict axial symmetry existed in the $[Ln(\beta_2\text{-}SiW_{11}O_{39})_2]^{13-}$ family, which was most readily apparent from the deviation from coplanarity of the two coordinating planes (deviation of angle between the normal vectors of the coordinating planes, ψ, from 0°). This deviation from axial symmetry appears to give rise to faster magnetic relaxation, probably by mixing the different wave functions and enhancing the rate of quantum tunneling through the energy barrier.

The $[Ln_4As_5W_{40}O_{144}(H_2O)_{10}(gly)_2]^{21-}$ family of complexes reported herein also displays axially compressed distorted D_{4d} local site symmetry at the rare earth centers, although the deviation from strictly axial symmetry is even greater than that observed for the $[Ln(\beta_2\text{-}SiW_{11}O_{39})_2]^{13-}$ family. This is particularly so for the Ln1 coordination environment characterized by an angle ψ (Table 3) of 5.1−7.1°, versus 0.9−2.2° for Ln2, 0° for $[Ln(W_5O_{18})_2]^{9-}$, and 0−4.1° for $[Ln(\beta_2\text{-}SiW_{11}O_{39})_2]^{13-}$.[8] Further, relevant deviation from ideal D_{4d} symmetry has been evidenced in our case by EPR spectra on both derivatives, resulting in doublets which are linear combinations of $|M_J \pm 4n\rangle$. This obviously affects the magnitude of the energy barrier estimated by dynamic susceptibility for the Dy derivative, due to the improved tunneling mechanism resulting from wave function mixing. If one considers the relatively small separation between the low-energy sublevels for compounds **2**−**4**, with the lowest energy levels separated by less than 25 cm^{-1} in each case, it is thus unsurprising that the energy barrier to magnetic relaxation determined for compound **3** is small. In any case, the observation of slow magnetic relaxation above 2.0 K for compound **3** and not for compound **4** is consistent with a larger energy barrier for the Dy compound.

CONCLUSIONS

The $[As_2W_{19}O_{67}(H_2O)]^{14-}$ polyanion is continuing to prove itself an invaluable starting material for the synthesis of higher nuclearity POMs, with structural reorientation of the precursor enabling complexation of the rare earth metals Gd, Tb, Dy, Ho, and Y. This has allowed isolation of the first POM-supported polynuclear lanthanoid-based SMM $(HDABCO)_8H_5Li_8[Dy_4As_5W_{40}O_{144}(H_2O)_{10}(gly)_2]\cdot 25H_2O$, for which an energy barrier to magnetization reversal of 3.9(1) K has been derived. Determination of the ligand field parameters indicates that the observed energy barrier arises from Ising-type magnetic anisotropy for this complex, which correlates with axial compression of the approximate local D_{4d} site symmetry at the Dy centers. The relatively small size of this energy barrier appears to result from the deviation from strictly axial local point symmetry, which is clearly evident from EPR studies on both Dy and Gd derivatives.

ASSOCIATED CONTENT

Supporting Information. X-ray crystallographic files in CIF format for **1**−**5**; details of modeling the magnetic susceptibility; infrared spectra of **1**−**5**; diagrams of the Ln coordination environments and crystal packing diagrams for compounds **1**−**5**; AC magnetic susceptibility data for **3**; Arrhenius plot for **3**; X-band EPR spectrum of **1**. This material is available free of charge via the Internet at http://pubs.acs.org.

AUTHOR INFORMATION

Corresponding Author

*E-mail: c.boskovic@unimelb.edu.au.

ACKNOWLEDGMENT

We thank the Australian Research Council for financial support.

REFERENCES

(1) (a) Pope, M. T. *Heteropoly and Isopoly Oxometalates*; Springer-Verlag: Berlin, 1983. (b) Borras-Almenar, J. J.; Coronado, E.; Müller, A.; Pope, M. T. (Eds), *Polyoxometalate Molecular Science*; Kluwer: Dordrecht, 2003.

(2) (a) Yamase, T. *Chem. Rev.* **1998**, *1*, 307.(b) Pope, M. T. *Compr. Coord. Chem. II* **2003**, *4*, 635 (c) Barats, C.; Leitus, G.; Popovitz-Biro, R.; Shimon, L. J. W.; Neumann, R. *Angew. Chem., Int. Ed.* **2008**, *47*, 9908.

(3) (a) Long, D. L.; Burkholder, E.; Cronin, L. *Chem. Soc. Rev.* **2007**, *36*, 105. (b) Hill, C. L. *Compr. Coord. Chem. II* **2003**, *4*, 679. (c) Kozhevnikov, I. V. *Chem. Rev.* **1998**, *98*, 171.

(4) (a) Bassil, B. S.; Kortz, U. *Z. Anorg. Allg. Chem.* **2010**, *636*, 2222. (b) Pope, M. T. *Handbook on the Physics and Chemistry of Rare Earths*; 2007; Vol. 38, pp 337−382.

(5) (a) Müller, A.; Peters, F.; Pope, M. T.; Gatteschi, D. *Chem. Rev.* **1998**, *98*, 239. (b) Coronado, E.; Galán-Mascarós, J. R.; Giménez-Saiz, C.; Gómez-García, C. J.; Falvello, L. R.; Delhaès, P. *Inorg. Chem.* **1998**, *37*, 2183. (c) Bi, L. H.; Kortz, U.; Dickman, M. H.; Nellutla, S.; Dalal, N. S.; Keita, B.; Nadjo, L.; Prinz, M.; Neumann, M. *J. Cluster Sci.* **2006**, *17*, 143. (d) Coronado, E.; Curreli, S.; Carlos Giménez-Saiz, C.; Gómez-García, C. J.; Alberola, A.; Canadell, E. *Inorg. Chem.* **2009**, *48*, 11314.

(6) (a) Clemente-Juan, J. M.; Coronado, E. *Coord. Chem. Rev.* **1999**, *193*−*195*, 361. (b) Kortz, U.; Müller, A.; van Slageren, J.; Schnack, J.; Dalal, N. S.; Dressel, M. S. *Coord. Chem. Rev.* **2009**, *253*, 2315.

(7) Ritchie, C.; Ferguson, A.; Nojiri, H.; Miras, H. N.; Song, Y.-F.; Long, D.-L.; Burkholder, E.; Murrie, M.; Kogerler, P.; Brechin, E. K.; Cronin, L. *Angew. Chem., Int. Ed.* **2008**, *47*, 5609.

(8) (a) Al Damen, M. A.; Clemente-Juan, J. M.; Coronado, E.; Martí-Gastaldo, C.; Gaita-Ariño, A. *J. Am. Chem. Soc.* **2008**, *130*, 8874. (b) Al Damen, M. A; Cardona-Serra, S.; Clemente-Juan, J. M.; Coronado, E.; Gaita-Ariño, A.; Marti-Gastaldo, C.; Luis, F.; Montero, O. *Inorg. Chem.* **2009**, *48*, 3467.

(9) Compaiin, J. −D.; Mialane, P.; Dolbecq, A.; Mbomekallé, I. M.; Marrot, J.; Sécheresse, F.; Riviere, E.; Rogez, G.; Wernsdorfer, W. *Angew. Chem., Int. Ed.* **2009**, *48*, 3077.

(10) (a) Gatteschi, D.; Sessoli, R. *Angew. Chem., Int. Ed.* **2003**, *42*, 268.(b) Winpenny, R. E., Ed. *Struct. Bonding (Berlin)* **2006**, *122*, entire volume. (c) Gatteschi, D.; Sessoli, R.; Villain, J. *Molecular Nanomagnets*; Oxford University Press: Oxford, 2006.

(11) (a) Sessoli, R.; Powell, A. K. *Coord. Chem. Rev.* **2009**, *253*, 2328. (b) Sorace, L.; Benelli, C.; Gatteschi, D. *Chem. Soc. Rev.* **2011**, *40*, 3092.

(12) (a) Ishikawa, N.; Iino, T.; Kaizu, Y. *J. Phys. Chem. A* **2002**, *106*, 9543. (b) Ishikawa, N.; Sugita, M.; Okubo, T.; Takana, N.; Iino, T.; Kaizu, Y. *Inorg. Chem.* **2003**, *42*, 2440. (c) Ishikawa, N.; Sugita, M.; Ishikawa, T.; Koshihara, S. Y.; Kaizu, Y. *J. Am. Chem. Soc.* **2003**, *125*, 8694. (d) Ishikawa, N.; Sugita, M.; Ishikawa, T.; Koshihara, S.; Kaizu, Y. *J.Phys. Chem. B* **2004**, *108*, 11265.

(13) (a) Jiang, S.-D.; Wang, B.-W.; Su, G.; Wang, Z.-M.; Gao, S. *Angew. Chem., Int. Ed.* **2010**, *49*, 7448. (b) Li, D.-P.; Wang, T.-W.; Li, C.-H.; Liu, D.-S.; Li, Y.-Z.; You, X.-Z. *Chem. Commun.* **2010**, *46*, 2929.

(14) (a) Gu, X.; Clérac, R.; Houri, A.; Xue, D. *Inorg. Chim. Acta* **2008**, *361*, 3873. (b) Gamer, M. T.; Lan, Y.; Roesky, P. W.; Powell, A. K.; Clérac, R. *Inorg. Chem.* **2008**, *47*, 6581. (c) Zheng, Y.-Z.; Lan, Y.; Anson, C. E.; Powell, A. K. *Inorg. Chem.* **2008**, *47*, 10813. (d) Lin, P.-H.; Burchell, T. J.; Clérac, R.; Murugesu, M. *Angew. Chem., Int. Ed.* **2008**, *47*, 8848. (e) Lin, P.-H.; Burchell, T. J.; Ungur, L.; Chibotaru, L. F.; Wernsdorfer, W.; Murugesu, M. *Angew. Chem., Int. Ed.* **2009**, *48*, 9489. (f) Gao, Y.; Xu, G.-F.; Zhao, L.; Tang, J.; Liu, Z. *Inorg. Chem.* **2009**, *48*, 11495. (g) Layfield, R. A.; McDouall, J. J. W.; Sulway, S. A.; Tuna, F.; Collison, D.; Winpenny, R. E. P. *Chem.—Eur. J.* **2010**, *16*, 4442.

(15) Papatriantafyllopoulou, C.; Wernsdorfer, W.; Abboud, K. A.; Christou, G. *Inorg. Chem.* **2011**, *50*, 421 and references therein.

(16) Hussain, F.; Gable, R. W.; Speldrich, M.; Kögerler, P.; Boskovic, C. *Chem. Commun.* **2009**, 328.

(17) Hussain, F.; Spingler, B.; Conrad, F.; Speldrich, M.; Kögerler, P.; Boskovic, C.; Patzke, G. R. *Dalton Trans.* **2009**, 4423.

(18) Ritchie, C.; Boskovic, C. *Cryst. Growth Des.* **2010**, *10*, 488.

(19) Ritchie, C.; Moore, E. G.; Speldrich, M.; Kögerler, P.; Boskovic, C. *Angew. Chem., Int. Ed.* **2010**, *49*, 7702.

(20) Wassermann, K.; Dickman, M. H.; Pope, M. T *Angew. Chem., Int. Ed. Engl.* **1997**, *36*, 1445.

(21) Zhang, C.; Howell, R. C.; Scotland, K. B.; Perez, F. G.; Todaro, L.; Francesconi, L. C. *Inorg. Chem.* **2004**, *43*, 7691.

(22) Zimmermann, M.; Belai, N.; Butcher, R. J.; Pope, M. T.; Chubarova, E. V.; Dickman, M. H.; Kortz, U. *Inorg. Chem.* **2007**, *46*, 1737.

(23) Chen, W.; Li, Y.; Wang, Y.; Wang, E.; Su, Z. *Dalton Trans.* **2007**, 4293.

(24) (a) Long, D. L.; Kögerler, P.; Farrugia, L. J.; Cronin, L. *Angew. Chem., Int. Ed.* **2003**, *42*, 4180. (b) Long, D. L.; Abbas, H.; Kögerler, P.; Cronin, L. *J. Am. Chem. Soc.* **2004**, *126*, 13880. (c) Ritchie, C.; Streb, C.; Thiel, J.; Mitchell, S. G.; Miras, H. N.; Long, D. L.; Boyd, T.; Peacock, R. D.; McGlone, T.; Cronin, L. *Angew. Chem., Int. Ed.* **2008**, *47*, 6881.

(25) Kortz, U.; Savelieff, M. G.; Bassil, B. S.; Dickman, M. H. *Angew. Chem., Int. Ed.* **2001**, *40*, 33.

(26) Speldrich, M.; Schilder, H.; Lueken, H.; Kögerler, P. *Isr. J. Chem.* **2011**, *51*, 215.

(27) Chang, S.; Li, Y. G.; Wang, E. B.; Xu, L.; Qin, C.; Wang, X. L.; Jin, H. *J. Mol. Struct.* **2008**, *875*, 462.

(28) Chang, S.; Zhang, Z.; Li, Y.; Yao, S.; Wang, E. *Aust. J. Chem.* **2010**, *63*, 680.

(29) (a) Bartis, J.; Sukal, S.; Dankova, M.; Kraft, E.; Kronzon, R.; Blumenstein, M.; Francesconi, L. C. *J. Chem. Soc., Dalton Trans.* **1997**, 1937. (b) Mitchell, S. G.; Streb, C.; Miras, H. N.; Boyd, T.; Long, D.-L.; Cronin, L. *Nat. Chem.* **2010**, *2*, 308–312.

(30) Brown, I. D.; Altermatt, D. *Acta Crystallogr.* **1985**, *B41*, 244.

(31) Müller, A.; Krickemeyer, E.; Dillinger, S.; Bogge, H.; Plass, W.; Proust, A.; Dloczik, L.; Menke, C.; Meyer, J.; Rohlfing, R. *Z. Anorg. Allg. Chem.* **1994**, *620*, 599.

(32) Shannon, R. D. *Acta Crystallogr.* **1976**, *A32*, 751.

(33) (a) Detusheva, L. G.; Kuznetsova, L. I.; Dovlitova, L. S.; Likholobov, V. A. *Russ. Chem. Bull. Int. Ed.* **2003**, *52*, 370. (b) Craciun, C.; Rusu, D.; Pop-Fanea, L.; Hossu, M.; Rusu, M.; David, L. *J. Radioanal. Nucl. Chem.* **2005**, *264*, 589.

(34) Muller, I. M.; Sheldrick, W. S. *Eur. J. Inorg. Chem.* **1998**, 1999.

(35) Nakamoto, K. *Infrared and Raman Spectra of Inorganic and Coordination Compounds, Part B*, 6th ed.; Wiley: New York, 2009.

(36) Tanner, P. A.; Kumar, V. V. R. K.; Jayasankar, C. K.; Reid, M. F. *J. Alloys Compd.* **1994**, *215*, 349.

(37) (a) Sytsma, J.; Murdoch, K. M.; Edelstein, N. M.; Boatner, L. A.; Abraham, M. M. *Phys. Rev. B* **1995**, *52*, 12668. (b) Shuskus, A. J. *Phys. Rev.* **1962**, *127*, 2022.

(38) Hüfner, S. *Optical Spectra of Transparent Rare Earth Compounds*; Academic Press, Inc.: New York, 1978.

(39) Kahn, M. L.; Ballou, R.; Porcher, P.; Kahn, O.; Sutter, J.-P. *Chem.—Eur. J.* **2002**, *8*, 525.

(40) (a) Cole, K. S.; Cole, R. H. *J. Chem. Phys.* **1941**, *9*, 341. (b) Dekker, C.; Arts, A. F. M.; Wijn, H. W.; van Duyneveldt, A. J.; Mydosh, J. A. *Phys. Rev. B* **1989**, *40*, 11243.

(41) (a) Niu, J.; Guo, D.; Zhao, J.; Wang, J. *New J. Chem.* **2004**, *28*, 980. (b) Szyczewski, A.; Lis, S.; Kruczynski, Z.; But, S.; Elbanowski, M.; Pietrzak, J. *J. Alloys Cmpd.* **1998**, *275*−*277*, 349. (c) Szyczewski, A.; Lis, S.; Kruczynski, Z.; But, S. *J. Alloys Cmpd.* **2002**, *341*, 307.

(42) (a) Pan, Y. M.; Fleet, M. E.; Chen, N.; Weil, J. A.; Nilges, M. *J. Can. Mineral.* **2002**, *40*, 1103. (b) Caneschi, A.; Dei, A.; Gatteschi, D.; Massa, C. A.; Pardi, L. A.; Poussereau, S.; Sorace, L. *Chem. Phys. Lett.* **2003**, *371*, 694.

(43) Abragam, A.; Bleaney, B. *Electron Paramagnetic Resonance of Transition Ions*; Dover Publications: New York, 1986.

(44) Lis, S. *J. Alloys Compd.* **2000**, *300*−*301*, 88.

(45) Baker, J. M.; Bleaney, B. *Proc. R. Soc. London A* **1958**, *245*, 156.